condensed matter

MDPI

Article

Pulse-Shape Discrimination with Machine Learning for CZT Detectors at DAΦNE Beam Test Facility

Simone Manti [1,*], Francesco Artibani [1,2], Leonardo Abbene [1,3], Massimiliano Bazzi [1], Manuele Bettelli [4], Giacomo Borghi [5,6], Damir Bosnar [7], Mario Bragadireanu [8], Antonino Buttacavoli [1,3], Marco Carminati [5,6], Alberto Clozza [1], Francesco Clozza [1,9], Luca De Paolis [1], Raffaele Del Grande [1,10], Kamil Dulski [1,11,12], Carlo Fiorini [5,6], Ivica Friščić [7], Gaetano Gerardi [3], Carlo Guaraldo [1], Mihai Iliescu [1], Masa Iwasaki [13], Alexander Khreptak [1,11,12], Johan Marton [14,15], Pawel Moskal [11,12], Hiroaki Ohnishi [16], Kristian Piscicchia [1,17], Fabio Principato [1,3], Alessandro Scordo [1], Francesco Sgaramella [1], Michał Silarski [11], Diana Sirghi [1,8,17], Florin Sirghi [1,8], Magdalena Skurzok [1,11,12], Antonio Spallone [1], Kairo Toho [1,16], Oton Vazquez Doce [1], Andrea Zappettini [4], Johann Zmeskal [14] and Catalina Curceanu [1,8]

1 Laboratori Nazionali di Frascati INFN, Via Enrico Fermi 54, 00044 Frascati, Italy
2 Dipartimento di Fisica, Università degli Studi di Roma Tre, Via della Vasca Navale 84, 00146 Roma, Italy
3 Department of Physics and Chemistry (DiFC), Emilio Segrè, University of Palermo, Viale delle Scienze, Edificio 17, 90128 Palermo, Italy
4 Istituto Materiali per l'Elettronica e il Magnetismo, Consiglio Nazionale delle Ricerche, Parco Area delle Scienze 37/A, 43124 Parma, Italy
5 Dipartimento di Elettronica, Informazione e Bioingegneria, Politecnico di Milano, Via Ponzio 34/5, 20133 Milano, Italy
6 INFN Sezione di Milano, Via Celoria 16, 20133 Milano, Italy
7 Department of Physics, Faculty of Science, University of Zagreb, Bijenička Cesta 32, 10000 Zagreb, Croatia
8 IFIN-HH, Institutul Național Pentru Fizică și Inginerie Nucleară Horia Hulubei, 30 Reactorului, 077125 Măgurele, Romania
9 Dipartimento di Fisica, Università degli Studi di Roma Tor Vergata, Via della Ricerca Scientifica 1, 00133 Roma, Italy
10 Faculty of Nuclear Sciences and Physical Engineering, Czech Technical University in Prague, Břehová 7, 115 19 Prague, Czech Republic
11 Faculty of Physics, Astronomy, and Applied Computer Science, Jagiellonian University, ul. S. Łojasiewicza 11, 30-348 Kraków, Poland
12 Center for Theranostics, Jagiellonian University, ul. Kopernika 40, 31-501 Kraków, Poland
13 Meson Science Laboratory, RIKEN Pioneering Research Institute, RIKEN (The Institute of Physical and Chemical Research), 2-1 Hirosawa, Wako 351-0198, Japan
14 Stefan Meyer Institute for Subatomic Physics, Austrian Academy of Sciences, Wiesingerstraße 4, 1010 Vienna, Austria
15 Atominstitut, Technische Universität Wien, Stadionallee 2, 1020 Vienna, Austria
16 Research Center for Accelerator and Radioisotope Science (RARiS), Tohoku University, 1-2-1 Mikamine, Taihaku-ku, Sendai 982-0826, Japan
17 Centro Ricerche Enrico Fermi, Museo Storico della Fisica e Centro Studi e Ricerche "Enrico Fermi", Via Panisperna 89/A, 00184 Roma, Italy
* Correspondence: simone.manti@lnf.infn.it

Check for updates

Academic Editor: Tullio Scopigno

Received: 21 September 2026
Revised: 7 October 2026
Accepted: 10 October 2026
Published: 13 October 2026

Copyright: © 2026 by the authors. Licensee MDPI, Basel, Switzerland. This article is an open access article distributed under the terms and conditions of the Creative Commons Attribution (CC BY) license.

Abstract

Cadmium zinc telluride (CZT) detectors offer versatility, operational simplicity, and room-temperature X- and gamma-ray spectroscopy, making them attractive for collider applications, yet their use under high-flux conditions remains limited. Here, we present a preliminary feature-based pulse-shape analysis employing machine learning on data acquired with a quasi-hemispherical CZT detector at the DAΦNE beam test facility of the National Laboratory of Frascati of INFN. A 300 MeV electron beam impinging on a lead target produced characteristic Pb X-rays together with a broad background extending up to the electron–positron annihilation region. Physically motivated temporal and morphological features were extracted from the recorded waveforms and used to distinguish nominal photon-like pulses from anomalous events. An XGBoost classifier trained and validated

on 10,000 labeled waveforms achieved an accuracy of approximately 97%, with most of its classification performance reached using only a few hundred labeled examples. The trained model was applied to more than 700,000 events, substantially reducing the spectral continuum and coincidence peaks, while preserving the characteristic Pb X-ray lines up to the 511 keV annihilation peak. These preliminary results demonstrate the potential of machine-learning-assisted pulse-shape discrimination for improving CZT spectroscopy in collider environments.

Keywords: CZT; BTF; pulse-shape analysis; machine learning; XGBoost

1. Introduction

High-resolution X- and gamma-ray spectroscopy is an essential tool in nuclear and particle physics [1,2], astrophysics [3], medical imaging [4], and plasma diagnostics [5]. Many of these applications require compact detection systems capable of operating over a broad energy range and under different experimental conditions. In particular, experiments characterized by high particle rates or intense electromagnetic backgrounds require detectors combining good spectroscopic performance, high detection efficiency, and stable operation over extended acquisition periods.

Cadmium zinc telluride (CZT) detectors represent an attractive solution for room-temperature photon spectroscopy [6]. Their high effective atomic number and density provide good detection efficiency, while their wide band gap allows operation without cryogenic cooling. These properties enable the development of compact detection systems with good spectroscopic performance, achieving an energy resolution of a few percent over energies ranging from a few keV to hundreds of keV [7,8], extending the possibility of detecting X-rays to gamma rays [9]. However, variations in charge transport and collection inside the crystal can produce different pulse morphologies, incomplete charge collection, and low-energy tails. Consequently, the recorded waveform contains information about the interaction and charge collection processes that is not fully represented by the reconstructed pulse amplitude alone.

The operation of CZT detectors in accelerator environments is particularly challenging because of the intense and complex electromagnetic background [7]. In addition to single photon interactions, the acquired data may contain multiple energy depositions, pile-up events, charged-particle interactions, electronic artifacts, accidental triggers, and saturated pulses. Some of these contributions overlap in energy with the signals of interest and cannot therefore be efficiently rejected using only the reconstructed energy. The identification of additional features sensitive to the event topology is consequently important for improving peak visibility and the signal-to-background ratio.

Within the SIDDHARTA-2 experiment [10] at the DAΦNE collider [11–13], CZT detectors are being investigated for the spectroscopy of intermediate-mass kaonic atoms. The characteristic transitions of these systems extend above the energy range primarily covered by the silicon drift detectors employed for light kaonic atoms. Previous measurements at DAΦNE demonstrated the feasibility of operating CZT detectors in a collider environment [14] and allowed several characteristic X-ray transitions to be observed in kaonic fluorine and copper [15]. Nevertheless, the residual beam-induced background limits the visibility of weak spectral features and represents an important challenge for future precision measurements, as planned by the EXKALIBUR project [16].

Pulse-shape analysis (PSA) provides a possible approach for distinguishing photon-like events from background contributions [17–20]. The temporal behavior of the detector

signal reflects the charge-collection process and may reveal multiple interactions, pile-up, anomalous rise profiles, saturation, or the absence of a physical pulse. Physically interpretable features, including the rise time, the number of peaks in the waveform derivative, and proxies for the interaction depth and charge-collection dynamics, can therefore be used to characterize the recorded events. Multivariate and machine learning (ML) methods can exploit the correlations among these features, potentially improving event classification compared to selection criteria based solely on individual features [21,22].

In this work, we present a preliminary PSA of data acquired with a quasi-hemispherical CZT detector with the DAΦNE beam test facility (BTF) at the National Laboratory of Frascati of INFN (INFN-LNF). Representative waveform morphologies were identified and characterized using a limited set of physically motivated pulse-shape features. The distributions of these features were investigated, and their capability to reject non-photon-like events was evaluated by comparing the amplitude spectrum before and after event selection. Particular attention was devoted to the visibility of the characteristic Pb X-ray lines and of the 511 keV annihilation peak. The purpose of this study is to demonstrate the feasibility of an interpretable waveform-based background suppression strategy for CZT detectors operating in an accelerator environment.

This paper is structured as follows: Section 2 describes the experimental setup, the CZT detection system, and the waveform-processing and feature extraction procedures. Section 3 presents the feature distributions, the preliminary classification results, and the effect of the event selection on the measured spectrum. Finally, Section 4 summarizes the main conclusions and outlines future developments.

2. Experimental Setup and Methods

The data used in this work were collected during a dedicated measurement campaign in 2026 at the DAΦNE BTF of the INFN-LNF, where the BTF provides pulsed electron or positron beams with adjustable energy and intensity [23]. For the present measurements, a 300 MeV electron beam impinged on a 1 mm-thick lead target. The beam–target interactions produced characteristic Pb X-rays, accompanied by bremsstrahlung and secondary particles. The resulting spectrum covered the characteristic Pb fluorescence lines (Lα, Kα and Kβ) and the higher-energy continuum, including the 511 keV electron–positron annihilation line. This configuration provided a controlled accelerator environment for investigating pulse-shape signatures associated with beam-induced backgrounds relevant to, although not fully representative of, those encountered at the interaction point of the DAΦNE collider, as in the SIDDHARTA-2 experiment.

The detection system consisted of a quasi-hemispherical CZT grown by the Traveling Heater Method by the REDLEN Technologiesdetector based on a $10 \times 10 \times 5$ mm^3 THM-CZT crystal [24,25]. The gold electrodes followed a quasi-hemispherical geometry, with a circular anode with a 750 µm diameter. During the measurements, the cathode was biased at -1050 V, while the anode was maintained at ground potential. The ambient temperature was approximately 22 °C. The crystal and its front-end electronics were enclosed in thin aluminum housing equipped with a 0.27 mm-thick entrance window. The quasi-hemispherical electrode geometry was employed to reduce the contribution of holes to the induced signal and to improve the charge-collection properties of the detector.

A 1 mm-thick Pb target was positioned approximately 10 cm above the detector entrance window, with its surface oriented at approximately 45° with respect to the incident beam (see Figure 1). The target-to-window distance was estimated from the setup geometry and was not directly measured. The detector was positioned close to the target to increase the efficiency in detecting the characteristic Pb X-rays. Two luminosity monitors were installed along the beam line, one before and one after the target. Each monitor consisted of

a plastic scintillator read out at both ends by photomultiplier tubes and was used to monitor the passage of the electron bunches. The detector signals were processed by a charge-sensitive preamplifier (CSP), whose output was fed directly to a CAEN VX2740 digitizer without additional amplification stages. The digitizer had an analog input bandwidth of 50 MHz, a 16-bit resolution, and a sampling rate of 125 MS/s. For each trigger, the pulse waveform and its corresponding amplitude were stored for offline analysis. The processed waveform contained 656 samples, corresponding to an approximately 5 μs time interval around the detector pulse. The pulse amplitude was subsequently converted into energy using a linear calibration based on the positions of the Pb $K\alpha$ and $K\beta$ lines.

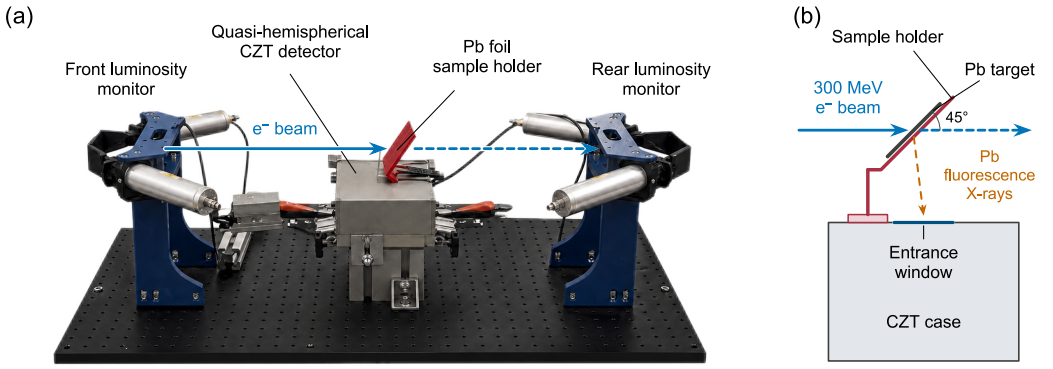


Figure 1. Experimental arrangement used for the measurements at the DAΦNE BTF of INFN-LNF. (**a**) Photograph of the setup, with the direction of the 300 MeV electron beam indicated. A 1 mm-thick Pb target was placed close to the CZT detector and between the front and rear luminosity monitors. Each luminosity monitor consisted of a plastic scintillator read out at both ends by photomultiplier tubes. (**b**) Schematic side view showing the sample holder, the Pb target oriented at 45° to the incident beam, and the CZT housing with its entrance window facing the target. The dashed orange arrow illustrates the path of fluorescence X-rays from the Pb target toward the detector. The schematic is not to scale.

The goal of PSA is to classify the acquired waveforms. Figure 2 shows some examples of pulses assigned to the normal and anomalous classes. Normal pulses display a single, regular rising edge followed by a stable plateau (see Figure 2a). Anomalous waveforms instead include pulses with multiple steps, pile-up, irregular charge collection, electronic disturbances, or no clearly identifiable physical pulse (see Figure 2b).

A set of 25 features was extracted from each waveform to quantify its amplitude, temporal development, and degree of regularity (see Table S1). These features included the pulse amplitude and integral, the rise time, the number of peaks in the first derivative, the waveform centroid and root mean square (RMS) width, the curvature, the charge-collection time, different rise-time ratios, and proxies for the depth of interaction (DOI), drift velocity, late charge collection, and ballistic deficit. Three representative features were considered in greater detail for the PSA: the rise time, the number of peaks in the waveform derivative, and the normalized RMS-width proxy, denoted as $\mathrm{DOI}_{\mathrm{RMS}}$. The rise time was calculated as $t_{90} - t_{10}$, where t_{10} and t_{90} are the first times at which the waveform reaches 10% and 90% of its maximum amplitude, respectively. The derivative was filtered using a median filter before identifying local maxima, reducing the number of peaks produced by high-frequency fluctuations. The temporal centroid t_c, its weighted RMS width σ_t, and the dimensionless $\mathrm{DOI}_{\mathrm{RMS}}$ feature were calculated within a single definition as

$$t_c = \frac{\sum_i w_i t_i}{\sum_i w_i}, \tag{1a}$$

$$\sigma_t = \sqrt{\frac{\sum_i w_i (t_i - t_c)^2}{\sum_i w_i}}, \tag{1b}$$

$$\mathrm{DOI}_{\mathrm{RMS}} = \frac{\sigma_t}{t_{90} - t_{10}}. \tag{1c}$$

where t_i is the time coordinate of the i-th sample, and w_i is the waveform value. The denominator $t_{90} - t_{10}$ represents the charge-collection-time proxy used in the analysis. The resulting feature characterizes the temporal spread of the collected charge relative to the pulse rise time. It is therefore sensitive to variations in the charge-collection process, although it should not be interpreted as a direct measurement of the physical interaction depth.

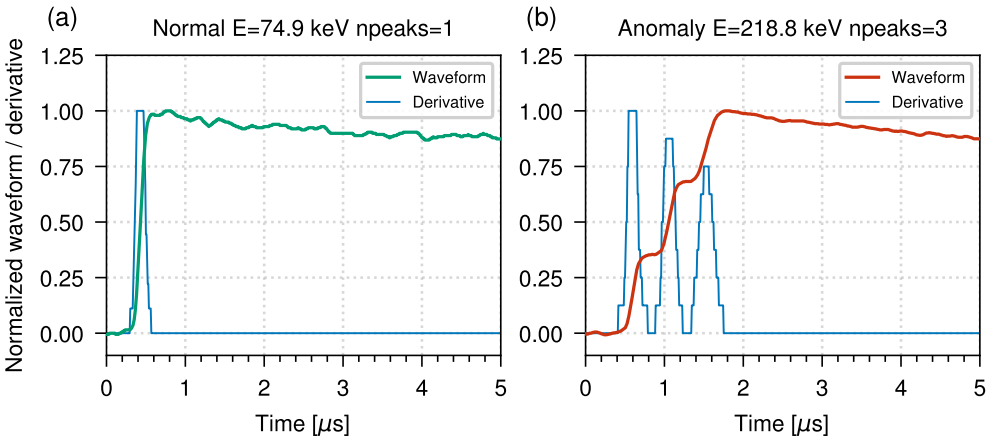


Figure 2. Representative waveforms classified as normal (**a**) and anomalous (**b**), with their median-filtered first derivatives superimposed. The normal event has an energy of 74.9 keV in the Pb Kα region and exhibits one derivative peak. The anomalous event has an energy of 218.8 keV in the triple-coincidence region and exhibits three derivative peaks.

Binary classification for the PSA was performed using the XGBoost algorithm. The analysis was implemented in Python 3.12 using the `scikit-learn` 1.4.2 and `xgboost` 3.2.0 [26] libraries. A subset of 10,000 events was used to train and evaluate the classifier. Initial labels were assigned based on the number of peaks in the first derivative and the rise time. Events were labeled as normal if the first derivative contained exactly one peak and the rise time was within 2σ from the mean of 0.2 µs. The labels were then visually inspected to identify and correct possible false positives and false negatives. The labeled dataset was divided into training and test sets using an 80/20 split. The XGBoost classifier consisted of 300 boosted decision trees with a maximum depth of four, a learning rate of 0.05, a row subsampling fraction of 0.8, and a feature subsampling fraction of 0.8 per tree. The classification threshold was selected to maximize the F1-score on the test set.

3. Preliminary Results and Discussion

The analysis was organized in three steps: first, the extraction of features from the acquired waveforms; then, the creation of the training set for training the XGBoost; and, finally, the classification of the entire data with the final selection in the total spectrum.

Figure 3 shows the distributions of the three features: the rise time, the number of peaks in the first derivative, and $\mathrm{DOI}_{\mathrm{RMS}}$ for the labeled dataset. Each feature provides some discrimination between the two classes, although their distributions partially overlap. As shown in Figure 3a, normal events are concentrated in a relatively narrow rise-time

interval around 0.2 µs. Anomalous events exhibit a broader distribution, with a component close to zero and a long tail extending beyond 1 µs. Very short rise times are consistent with noise-like pulses, whereas longer rise times may reflect irregular charge collection, pile-up, or temporally separated energy depositions. The number of peaks in the first derivative, shown in Figure 3b, characterizes the structure of the rising edge. Most normal events exhibit a single peak, consistent with a smooth, regular rise. Anomalous events more frequently exhibit either no identifiable peak or multiple peaks, the latter being consistent with multi-step waveforms, pile-up, or noise. Some overlap remains, particularly for low-energy events, in which noise-induced fluctuations along the rising edge can produce additional derivative peaks. The combined feature $\mathrm{DOI}_{\mathrm{RMS}}$ defined in (1) and shown in Figure 3c, exhibits the clearest separation between the two classes. Normal events predominantly populate intermediate and high values, with a maximum around 8–9, whereas anomalous events concentrate mainly below $\mathrm{DOI}_{\mathrm{RMS}} \simeq 4$. Nevertheless, residual overlap limits the discrimination achievable with a single threshold. These distributions therefore motivated the development of a multivariate approach that exploits the complementary information and correlations among the three waveform features using ML methods.

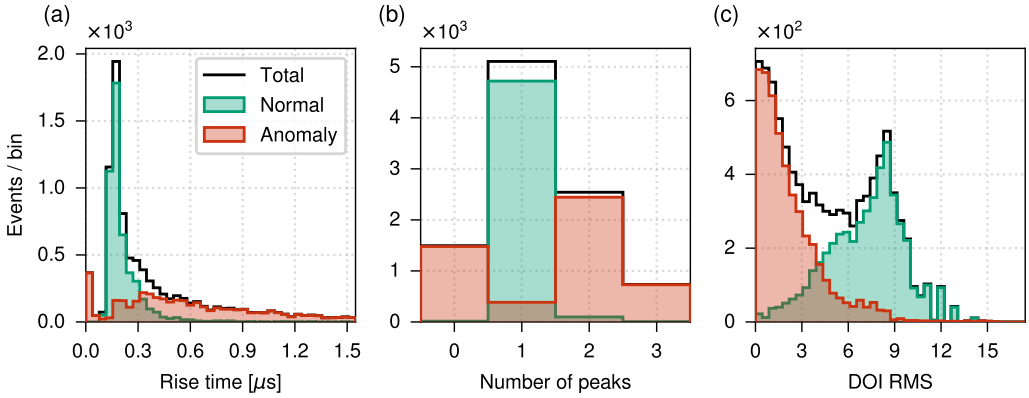


Figure 3. Distributions of three representative pulse-shape features for the manually validated normal (green) and anomalous (red) waveforms; the black histogram represents the complete labeled sample: (**a**) rise time, (**b**) number of peaks in the first derivative, and (**c**) normalized temporal-width proxy $\mathrm{DOI}_{\mathrm{RMS}}$.

ML was used to classify waveforms based on pulse-shape features. XGBoost was trained on a subset of the acquired events, with initial labels assigned using feature-based criteria (see Section 2) and subsequently refined through visual inspection. The classification performance obtained using the complete feature set is reported in Figure 4 and the importance of each feature in Table S1. The receiver operating characteristic (ROC) curves, evaluated on the fixed test sample, are shown in Figure 4a. XGBoost achieved an area under the curve (AUC) of 0.996 and an accuracy of 96.8%. To compare ML with respect to using feature selection, we also used $\mathrm{DOI}_{\mathrm{RMS}}$ as a threshold, achieving an AUC of only 0.85, exhibiting the advantage of exploiting the entire feature correlation for classification. We further explored the dependence of XGBoost accuracy on the number of training events, as shown in Figure 4b. With only a few training events, the mean accuracy was approximately 79% and exhibited a relatively large variation among the different stratified samples. The accuracy increased to approximately 93% with a few hundred of training events and approached 97% when several thousand labeled waveforms were used. The observed saturation indicates that most of the classification performance can already be obtained with a few hundred labeled events, although a larger training sample improves both accuracy and stability. Selecting the classification threshold by maximizing the F1-score on a separate validation set yielded a test accuracy of 96.5%.

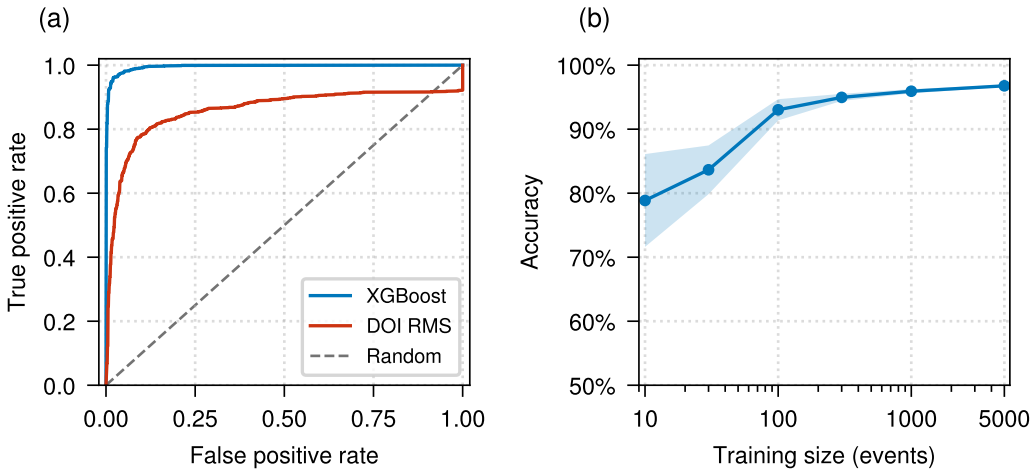


Figure 4. (**a**) The ROC for XGBoost (blue) and the curve (red) obtained using the DOI_{RMS} feature as the threshold for the classifier. (**b**) XGBoost classification accuracy as a function of the number of training events. The points and shaded region in (**b**) represent the mean and standard deviation obtained from ten independently drawn stratified training subsets, respectively.

After the classification performance was evaluated on the test sample, the final XGBoost model was then applied to 790,700 events. This selection accepted 381,351 events, corresponding to 48.2% of the complete dataset. Figure 5 compares the calibrated spectrum of the complete dataset with that obtained after the XGBoost selection. The two distributions use the same acquisition exposure and energy binning and are reported as absolute counts. The unselected spectrum contains the characteristic Pb $L\alpha$, $K\alpha$, and $K\beta$ lines, together with double- and triple-coincidence structures at approximately 150 and 220 keV, respectively, and the electron–positron annihilation peak around 511 keV. XGBoost selection produces a broad reduction of the continuum over the entire investigated energy range while preserving the main characteristic lines. The double- and triple-coincidence regions are suppressed more strongly than the isolated Pb K lines, consistently with the presence of multi-step or pile-up waveforms among the rejected events. A reduction in the high-energy continuum is also observed around the 511 keV region, where the annihilation peak remains visible after the selection, with improved signal-to-noise ratio. These results demonstrate that the information encoded in the waveform features can be used to improve the relative visibility of the spectral structures in the presence of an intense accelerator-induced background.

This preliminary study demonstrates that a few hundred manually labeled waveforms are sufficient to achieve a classification accuracy above 90% relative to the assigned labels and suppress the spectral continuum while preserving the main spectral structures. Further validation across independent acquisitions, detector setups, and beam conditions is needed to establish generalizability. Future developments could employ one-dimensional convolutional neural networks (CNNs) to exploit waveform morphology directly. Integration into the DAQ could enable online event rejection without routinely storing full waveforms, potentially reducing processing time by bypassing explicit feature extraction; this advantage should be verified through latency benchmarks. CNN implementation in FPGA-based acquisition systems provides a precedent for this approach [27]. ML interpretability methods, like feature importance and SHAP analysis [28], could clarify the features driving the current classifier, while Grad-CAM adapted to one-dimensional signals could identify waveform regions relevant to CNN predictions [29]. Finally, Monte Carlo simulations coupled with charge transport, signal formation, and electronic response models could provide physically motivated training labels, reducing reliance on manual annotation, provided that simulated waveforms are validated against measurements [30–32].

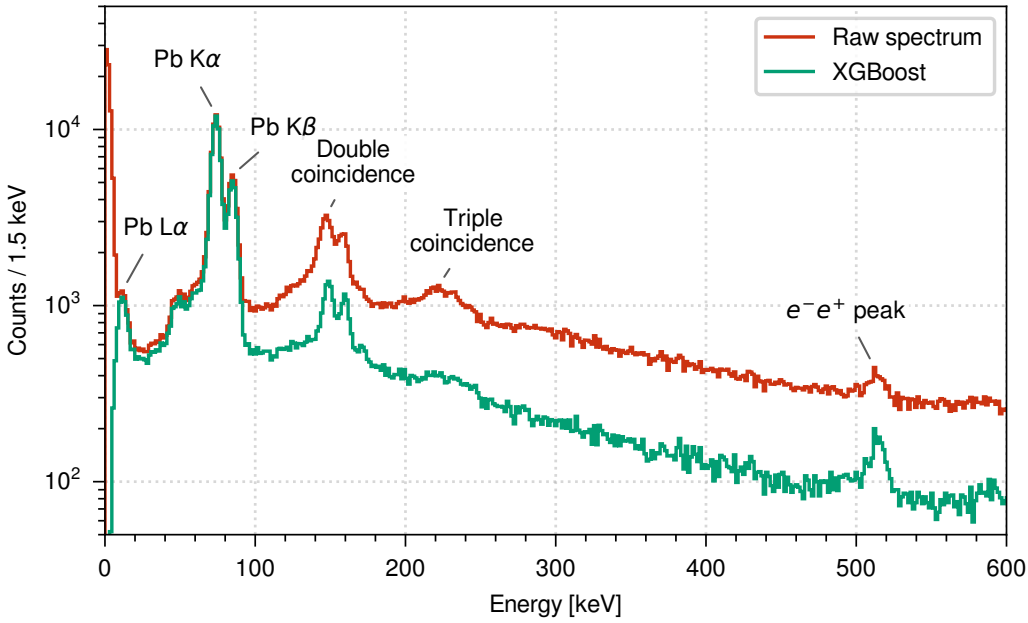


Figure 5. Calibrated CZT energy spectrum before event selection (red) and after retaining events classified as normal by the feature-based XGBoost model (green). The same acquisition exposure and an energy bin width of 1.5 keV are used for both distributions. The characteristic Pb lines, the double- and triple-coincidence structures, and the 511 keV electron–positron annihilation peak are indicated.

4. Conclusions

This work demonstrates the feasibility of feature-based pulse-shape analysis for background suppression in a quasi-hemispherical CZT detector operated at the DAΦNE BTF of INFN-LNF. By combining temporal and morphological waveform features, the XGBoost classifier achieved an AUC of 0.996 and an accuracy of 96.8% on the fixed test sample, with accuracies above 90% obtained using only a few hundred labeled waveforms. The final model, trained on the complete labeled sample and applied to 790,700 events, retained 48.2% of the data and substantially reduced the spectral continuum while maintaining the visibility of the characteristic Pb lines and the 511 keV annihilation peak. The preferential suppression of the double- and triple-coincidence structures is consistent with the rejection of multi-step and pile-up waveforms. These preliminary results indicate the potential of machine-learning-assisted pulse-shape discrimination for CZT spectroscopy in accelerator environments and motivate further validation for future collider applications.

The classification metrics quantify agreement with morphology-based labels rather than independently verified interaction topologies. Further validation will focus on the energy dependence of signal efficiency and background rejection, including the role of amplitude-related features, and on stability across independent acquisitions and detector conditions. Complementary studies using simulated waveforms will support the physical interpretation of the selected events and the development of the method toward quantitative spectroscopy and online event selection.

Supplementary Materials: The following supporting information can be downloaded at https://www.mdpi.com/article/10.3390/condmat11040038/s1, Table S1: The names and normalized gain-based importance of the 25 input features used by the XGBoost classifier.

Author Contributions: Conceptualization, S.M., F.A., C.C. and A.S. (Alessandro Scordo); methodology, S.M., F.A., L.A. and A.B.; software, S.M., F.A., G.B., M.C. and C.F.; validation, S.M., F.A., L.A., A.B. and A.S. (Alessandro Scordo); formal analysis, S.M., F.A., F.C. and F.S. (Francesco Sgaramella); investigation, S.M., F.A., M.B. (Massimiliano Bazzi), D.B., M.B. (Mario Bragadireanu), A.C., L.D.P., R.D.G., K.D., I.F., G.G., C.G., M.I. (Mihai Iliescu), M.I. (Masa Iwasaki), A.K., J.M., P.M., H.O., K.P.,

F.P., F.S. (Francesco Sgaramella), M.S. (Michał Silarski), D.S., F.S. (Florin Sirghi), M.S. (Magdalena Skurzok), A.S. (Antonio Spallone), K.T., O.V.D. and J.Z.; resources, M.B. (Massimiliano Bazzi), M.B. (Manuele Bettelli), D.B., M.B. (Mario Bragadireanu), R.D.G., K.D., M.I. (Masa Iwasaki), J.M., P.M., H.O., D.S., F.S. (Florin Sirghi), M.S. (Magdalena Skurzok), A.S. (Antonio Spallone), K.T., A.Z., J.Z. and C.C.; data curation, S.M., F.A., A.C., C.G., M.I. (Mihai Iliescu) and O.V.D.; writing—original draft preparation, S.M. and F.A.; writing—review and editing, L.A., M.B. (Massimiliano Bazzi), M.B. (Manuele Bettelli), G.B., D.B., M.B. (Mario Bragadireanu), A.B., M.C., A.C., F.C., L.D.P., R.D.G., K.D., C.F., I.F., G.G., C.G., M.I. (Mihai Iliescu), M.I. (Masa Iwasaki), A.K., J.M., P.M., H.O., K.P., F.P., A.S. (Alessandro Scordo), F.S. (Francesco Sgaramella), M.S. (Michał Silarski), D.S., F.S. (Florin Sirghi), M.S. (Magdalena Skurzok), A.S. (Antonio Spallone), K.T., O.V.D., A.Z., J.Z. and C.C.; visualization, S.M. and F.A.; supervision, C.C., A.S. (Alessandro Scordo), L.A. and A.B.; project administration, S.M., F.A., A.S. (Alessandro Scordo) and C.C.; funding acquisition, C.C., A.S. (Alessandro Scordo), M.I. (Masa Iwasaki) and P.M. All authors have read and agreed to the published version of the manuscript.

Funding: This work was supported by the INFN KAONNIS project; the Austrian Science Fund (FWF), grants P24756-N20 and P33037-N; the Croatian Science Foundation, project IP-2022-10-3878; the EU STRONG-2020 project, Grant Agreement No. 824093; the EU Horizon 2020 Programme under the Marie Skłodowska-Curie Actions, Grant Agreement No. 754496; the Japan Society for the Promotion of Science through JSPS KAKENHI grants JP18H05402 and JP22H04917; the Polish Ministry of Science and Higher Education, grant 7150/E-338/M/2018; the Polish National Agency for Academic Exchange, grant PPN/BIT/2021/1/00037; and COST Action CA24131–ENRICH, supported by COST (European Cooperation in Science and Technology, https://www.cost.eu/). We gratefully acknowledge the Polish high-performance computing infrastructure PLGrid (HPC Center: ACK Cyfronet AGH) for providing computing facilities and support within computational grant PLG/2025/018524.

Data Availability Statement: The data supporting the findings of this study are available from the corresponding author upon reasonable request.

Acknowledgments: We thank Luca Gennaro Foggetta and Eleonora Diociaiuti for their tailored beam setups and scientific support. We also extend our gratitude to the DAΦNE operators and LINAC service for maintaining uptime in BTF injections. We thank C. Capoccia from INFN-LNF and H. Schneider, L. Stohwasser and D. Pristauz-Telsnigg from the Stefan Meyer Institute for their fundamental contributions to the design and construction of the SIDDHARTA-2 setup. Special thanks are extended to Catia Milardi for her continued support and contribution during data taking.

Conflicts of Interest: The authors declare no conflicts of interest.

References

1. Eberth, J.; Simpson, J. From Ge(Li) Detectors to Gamma-Ray Tracking Arrays–50 Years of Gamma Spectroscopy with Germanium Detectors. *Prog. Part. Nucl. Phys.* **2008**, *60*, 283–337. [CrossRef]
2. Gotta, D. Precision Spectroscopy of Light Exotic Atoms. *Prog. Part. Nucl. Phys.* **2004**, *52*, 133–195. [CrossRef]
3. Harrison, F.A.; Craig, W.W.; Christensen, F.E.; Hailey, C.J.; Zhang, W.W.; Boggs, S.E.; Stern, D.; Cook, W.R.; Forster, K.; Giommi, P.; et al. The Nuclear Spectroscopic Telescope Array (NuSTAR) High-Energy X-Ray Mission. *Astrophys. J.* **2013**, *770*, 103. [CrossRef]
4. Taguchi, K.; Iwanczyk, J.S. Vision 20/20: Single-Photon-Counting X-Ray Detectors in Medical Imaging. *Med. Phys.* **2013**, *40*, 100901. [CrossRef] [PubMed]
5. Renner, O.; Rosmej, F.B. Challenges of X-Ray Spectroscopy in Investigations of Matter under Extreme Conditions. *Matter Radiat. Extrem.* **2019**, *4*, 024201. [CrossRef]
6. Iniewski, K. *CdTe and CdZnTe Materials: Material Properties and Applications*; Springer Nature: Berlin/Heidelberg, Germany, 2024.
7. Mele, F.; Quercia, J.; Abbene, L.; Benassi, G.; Bettelli, M.; Buttacavoli, A.; Principato, F.; Zappettini, A.; Bertuccio, G. Advances in High-Energy-Resolution CdZnTe Linear Array Pixel Detectors with Fast and Low Noise Readout Electronics. *Sensors* **2023**, *23*. [CrossRef] [PubMed]
8. Abbene, L.; Principato, F.; Gerardi, G.; Buttacavoli, A.; Cascio, D.; Bettelli, M.; Amadè, N.S.; Seller, P.; Veale, M.C.; Fox, O.; et al. Room-Temperature X-Ray Response of Cadmium–Zinc–Telluride Pixel Detectors Grown by the Vertical Bridgman Technique. *J. Synchrotron Radiat.* **2020**, *27*, 319–328. [CrossRef] [PubMed]

9. Eisen, Y.; Shor, A. CdTe and CdZnTe Materials for Room-Temperature X-Ray and Gamma Ray Detectors. *J. Cryst. Growth* **1998**, *184–185*, 1302–1312. [CrossRef]
10. Sirghi, F.; Iliescu, M.; Abbene, L.; Amsler, C.; Bazzi, M.; Borghi, G.; Bosnar, D.; Bragadireanu, M.; Buttacavoli, A.; Carminati, M..; et al. SIDDHARTA-2 Apparatus for Kaonic Atoms Research. *J. Instrum.* **2024**, *19*, P11006. [CrossRef]
11. Milardi, C.; Alesini, D.; Bini, S.; Blanco-García, O.; Boscolo, M.; Buonomo, B.; Cantarella, S.; Caschera, S.; Castorina, G.; Chavanne, J.; et al. Preparation Activity for the SIDDHARTA-2 Run at DAΦNE. In *Proceedings of the 9th International Particle Accelerator Conference (IPAC2018)*; JACOW Publishing: Geneva, Switzerland, 2018; pp. 334–337. [CrossRef]
12. Milardi, C.; Alesini, D.; Blanco-García, O.; Boscolo, M.; Buonomo, B.; Cantarella, S.; Chavanne, J.; D'Uffizi, A.; De Santis, A.; Di Giulio, C.; et al. DAΦNE Commissioning for the SIDDHARTA-2 Experiment. In *Proceedings of the 12th International Particle Accelerator Conference (IPAC2021)*; JACOW Publishing: Geneva, Switzerland, 2021; pp. 1322–1325. [CrossRef]
13. Milardi, C.; Alesini, D.; Blanco-García, O.; Boscolo, M.; Buonomo, B.; Cantarella, S.; Chavanne, J.; D'Uffizi, A.; De Santis, A.; Di Giulio, C.; et al. DAΦNE Operation Strategy for the Observation of Kaonic Deuterium. In *Proceedings of the 15th International Particle Accelerator Conference (IPAC2024)*; JACoW Publishing: Geneva, Switzerland, 2024; pp. 2504–2507. [CrossRef]
14. Scordo, A.; Abbene, L.; Artibani, F.; Bazzi, M.; Bettelli, M.; Bosnar, D.; Borghi, G.; Bragadireanu, M.; Buttacavoli, A.; Cargnelli, M.; et al. CdZnTe Detectors Tested at the DAΦNE Collider for Future Kaonic Atoms Measurements. *Nucl. Instrum. Methods Phys. Res. Sect. A Accel. Spectrometers Detect. Assoc. Equip.* **2024**, *1060*, 169060. [CrossRef]
15. Artibani, F.; Manti, S.; Abbene, L.; Buttacavoli, A.; Bettelli, M.; Gerardi, G.; Principato, F.; Zappettini, A.; Bazzi, M.; Borghi, G.; et al. Kaonic Copper and Fluorine Absolute Yields Measurement with a CZT-Based Detection System at DAΦNE. *J. Phys. G Nucl. Part. Phys.* **2026**, *53*, 095102. [CrossRef]
16. Manti, S.; Khreptak, A.; Marton, J.; Moskal, P.; Ohnishi, H.; Pischicchia, K.; Principato, F.; Scordo, A.; Sgaramella, F.; Silarski, M.; et al. EXKALIBUR: Towards a Kaonic Atoms Periodic Table to Test Fundamental Interactions. *Acta Phys. Pol. A* **2025**, *148*, S89–S89. [CrossRef]
17. McGrath, J.; Fulton, B.R.; Joshi, P.; Davies, P.; Muenstermann, D.; Schulz, O.; Zuber, K.; Freer, M. Detecting Multi-Hit Events in a CdZnTe Coplanar Grid Detector Using Pulse Shape Analysis: A Method for Improving Background Rejection in the COBRA $0\nu\beta\beta$ Experiment. *Nucl. Instrum. Methods Phys. Res. Sect. A Accel. Spectrometers Detect. Assoc. Equip.* **2010**, *615*, 57–61. [CrossRef]
18. Nakhostin, M.; Podolyak, Z.; Sellin, P.J. Application of Pulse-Shape Discrimination to Coplanar CdZnTe Detectors. *Nucl. Instrum. Methods Phys. Res. Sect. A Accel. Spectrometers Detect. Assoc. Equip.* **2013**, *729*, 541–545. [CrossRef]
19. Fritts, M.; Tebrügge, J.; Durst, J.; Ebert, J.; Gößling, C.; Göpfert, T.; Gehre, D.; Hagner, C.; Heidrich, N.; Homann, M.; et al. Pulse-Shape Discrimination of Surface Events in CdZnTe Detectors for the COBRA Experiment. *Nucl. Instrum. Methods Phys. Res. Sect. A Accel. Spectrometers Detect. Assoc. Equip.* **2014**, *749*, 27–34. [CrossRef]
20. Abbene, L.; Gerardi, G. Performance Enhancements of Compound Semiconductor Radiation Detectors Using Digital Pulse Processing Techniques. *Nucl. Instrum. Methods Phys. Res. Sect. A Accel. Spectrometers Detect. Assoc. Equip.* **2011**, *654*, 340–348. [CrossRef]
21. Holl, P.; Hauertmann, L.; Majorovits, B.; Schulz, O.; Schuster, M.; Zsigmond, A.J. Deep Learning Based Pulse Shape Discrimination for Germanium Detectors. *Eur. Phys. J. C* **2019**, *79*, 450. [CrossRef]
22. Manti, S.; Yip, S.; Bazzi, M.; Bortolotti, N.; Bragadireanu, M.; Carnevali, I.; Clozza, A.; De Paolis, L.; Del Grande, R.; Guaraldo, C.; et al. Machine-Learning-Enhanced Event Selection for BEGe Detectors in the VIP Experiment. *J. Instrum.* **2026**, *21*, P01036. [CrossRef]
23. Foggetta, L.; Belli, M.; Buonomo, B.; Cardelli, F.; Ceccarelli, R.; Cecchinelli, A.; Clementi, R.; Di Giovenale, D.; Di Giulio, C.; Piermarini, G.; et al. The Extended Operative Range of the LNF LINAC and BTF Facilities. In Proceedings of the 12th International Particle Accelerator Conference, Campinas, SP, Brazil, 24–28 May 2021. [CrossRef]
24. Chen, H.; Awadalla, S.A.; Mackenzie, J.; Redden, R.; Bindley, G.; Bolotnikov, A.E.; Camarda, G.S.; Carini, G.; James, R.B. Characterization of Traveling Heater Method (THM) Grown \hboxCd_0.9\hboxZn_0.1\hboxTe Crystals. *IEEE Trans. Nucl. Sci.* **2007**, *54*, 811–816. [CrossRef]
25. Buttacavoli, A.; Principato, F.; Gerardi, G.; Cascio, D.; Raso, G.; Bettelli, M.; Zappettini, A.; Seller, P.; Veale, M.C.; Abbene, L. Incomplete Charge Collection at Inter-Pixel Gap in Low- and High-Flux Cadmium Zinc Telluride Pixel Detectors. *Sensors* **2022**, *22*, 1441. [CrossRef] [PubMed]
26. Chen, T.; Guestrin, C. XGBoost: A Scalable Tree Boosting System. In *Proceedings of the 22nd ACM SIGKDD International Conference on Knowledge Discovery and Data Mining*; ACM: New York, NY, USA, 2016; pp. 785–794. [CrossRef]
27. Astrain, M.; Ruiz, M.; Stephen, A.V.; Sarwar, R.; Carpeño, A.; Esquembri, S.; Murari, A.; Belli, F.; Riva, M. Real-Time Implementation of the Neutron/Gamma Discrimination in an FPGA-Based DAQ MTCA Platform Using a Convolutional Neural Network. *IEEE Trans. Nucl. Sci.* **2021**, *68*, 2173–2178. [CrossRef]
28. Lundberg, S.M.; Erion, G.; Chen, H.; DeGrave, A.; Prutkin, J.M.; Nair, B.; Katz, R.; Himmelfarb, J.; Bansal, N.; Lee, S.I. From Local Explanations to Global Understanding with Explainable AI for Trees. *Nat. Mach. Intell.* **2020**, *2*, 56–67. [CrossRef] [PubMed]

29. Selvaraju, R.R.; Cogswell, M.; Das, A.; Vedantam, R.; Parikh, D.; Batra, D. Grad-CAM: Visual Explanations From Deep Networks via Gradient-Based Localization. In Proceedings of the IEEE International Conference on Computer Vision, Venice, Italy, 22–29 October 2017; pp. 618–626.
30. Bettelli, M.; Amadè, N.S.; Calestani, D.; Garavelli, B.; Pozzi, P.; Macera, D.; Zanotti, L.; Gonano, C.A.; Veale, M.C.; Zappettini, A. A First Principle Method to Simulate the Spectral Response of CdZnTe-Based X- and Gamma-Ray Detectors. *Nucl. Instrum. Methods Phys. Res. Sect. A Accel. Spectrometers Detect. Assoc. Equip.* **2020**, *960*, 163663. [CrossRef]
31. Vicini, V.; Zanettini, S.; Sarzi Amadè, N.; Grill, R.; Zambelli, N.; Calestani, D.; Zappettini, A.; Abbene, L.; Bettelli, M. Optimization of Quasi-Hemispherical CdZnTe Detectors by Means of First Principles Simulation. *Sci. Rep.* **2023**, *13*, 3212. [CrossRef] [PubMed]
32. Yu, S.; He, L.; Li, Y.; Tian, Y.; Yang, M. Pulse Shape Discrimination Using a Convolutional Neural Network in an Inverted Coaxial Point Contact HPGe Detector. *Nucl. Instrum. Methods Phys. Res. Sect. A Accel. Spectrometers Detect. Assoc. Equip.* **2025**, *1072*, 170219. [CrossRef]

Disclaimer/Publisher's Note: The statements, opinions and data contained in all publications are solely those of the individual author(s) and contributor(s) and not of MDPI and/or the editor(s). MDPI and/or the editor(s) disclaim responsibility for any injury to people or property resulting from any ideas, methods, instructions or products referred to in the content.